

## A LOCALLY CONSERVATIVE EULERIAN–LAGRANGIAN METHOD FOR A MODEL TWO-PHASE FLOW PROBLEM IN A ONE-DIMENSIONAL POROUS MEDIUM\*

TODD ARBOGAST<sup>†</sup>, CHIEH-SEN HUANG<sup>‡</sup>, AND THOMAS F. RUSSELL<sup>§</sup>

**Abstract.** Motivated by possible generalizations to more complex multiphase multicomponent systems in higher dimensions, we develop an Eulerian–Lagrangian numerical approximation for a system of two conservation laws in one space dimension modeling a simplified two-phase flow problem in a porous medium. The method is based on following tracelines, so it is stable independent of any CFL constraint. The main difficulty is that it is not possible to follow individual tracelines independently. We approximate tracing along the tracelines by using local mass conservation principles and self-consistency. The two-phase flow problem is governed by a system of equations representing mass conservation of each phase, so there are two local mass conservation principles. Our numerical method respects both of these conservation principles over the computational mesh (i.e., locally), and so is a fully conservative traceline method. We present numerical results that demonstrate the ability of the method to handle problems with shocks and rarefactions, and to do so with very coarse spatial grids and time steps larger than the CFL limit.

**Key words.** advection-diffusion, characteristics, streamlines, tracelines, local conservation, two-phase, shocks, rarefactions

**AMS subject classifications.** 65M08, 65M25, 76M12, 76S05, 76T99

**DOI.** 10.1137/090778079

**1. Introduction.** We consider the problem of numerical approximation of a system of two conservation laws modeling a simplified two-phase flow problem in a one-dimensional porous medium. We develop an Eulerian–Lagrangian traceline method with particular attention given to local mass conservation principles and stability independence of any CFL constraint [20], so that large time steps can be used, only subject to accuracy concerns. The two-phase flow problem is governed by a system of two equations representing mass conservation of each phase [5, 21, 8], so there are two local mass conservation principles, one for each phase. Numerical methods should respect both of these conservation principles over the computational mesh (i.e., locally). The main difficulty for traceline methods is that it is not possible

---

\*Submitted to the journal’s Methods and Algorithms for Scientific Computing section November 23, 2009; accepted for publication (in revised form) March 20, 2012; published electronically July 12, 2012. This work was performed by an employee of the U.S. Government or under U.S. Government contract. The U.S. Government retains a nonexclusive, royalty-free license to publish or reproduce the published form of this contribution, or allow others to do so, for U.S. Government purposes. Copyright is owned by SIAM to the extent not limited by these rights.

<http://www.siam.org/journals/sisc/34-4/77807.html>

<sup>†</sup>Department of Mathematics, The University of Texas at Austin, 2515 Speedway, Stop C1200, Austin, TX 78712-1202, and Institute for Computational Engineering and Sciences, The University of Texas at Austin, 201 East 24th St., Stop C0200, Austin, TX 78712-1229 (arbogast@ices.utexas.edu). This author was supported in part by U.S. National Science Foundation grants DMS-0713815 and DMS-0835745, the King Abdullah University of Science and Technology (KAUST) Academic Excellence Alliance program, and the Mathematics Research Promotion Center of Taiwan.

<sup>‡</sup>Department of Applied Mathematics and National Center for Theoretical Sciences, National Sun Yat-sen University, Kaohsiung 804, Taiwan, Republic of China (huangcs@math.nsysu.edu.tw). This author was supported in part under Taiwan National Science Council grants 96-2115-M-110-002-MY3 and 99-2115-M-110-006-MY3.

<sup>§</sup>Division of Mathematical Sciences, U.S. National Science Foundation, 4201 Wilson Blvd., Arlington, VA 22230 (trussell@nsf.gov).

to follow individual tracers independently. We achieve approximate tracing along the tracers by using both local mass conservation principles and self-consistency.

Eulerian numerical methods based on fixed grids, such as Godunov's method [20], are locally mass conservative for each phase by design, since the volumes of the fixed grid elements do not change in time. However, they are subject to the CFL constraint.

Lagrangian methods, such as moving mesh and characteristic methods, have been developed to approximate single-phase, linear transport problems without the need to enforce any CFL constraint. These problems have two miscible fluids, a tracer and the ambient fluid. Like our two-phase problem, they are governed by two conservation principles. The Eulerian-Lagrangian methods use Lagrangian ideas to advance the solution in time, but the solution is projected back to a fixed Eulerian frame each time step. Among such methods, Douglas and Russell introduced the Modified Method of Characteristics in 1982 [14, 15, 11] (see also [22]), but it violates *both* local mass constraints. Methods that conserve the tracer fluid locally appeared in the early 1990s [7, 1, 4, 10, 12, 29, 30, 28], but these methods violate the local mass constraint for the ambient fluid. Two-phase versions were also developed (see, e.g., [13, 16]), but fail to conserve both fluids locally.

The volume corrected characteristics-mixed method (VCCMM) was introduced in [2] by two of the current authors. Very briefly, VCCMM computes the mass distribution on the Eulerian computational mesh at a time level  $t^{n+1}$  by three main steps. Step 1 is to trace (approximately) each grid element  $E$  back in time to the previous time  $t^n$  along the Lagrangian characteristics or tracers of the flow. Step 2 is then to correct the volume of the trace-back elements  $\tilde{E}$  so each agrees with the volume of  $E$  (of course maintaining the property that the entire corrected trace-back mesh tessellates space). Finally, Step 3 is to sum the tracer mass in each  $\tilde{E}$ , which is assumed transported to the original grid element  $E$  at time  $t^{n+1}$ . Step 3 ensures local mass conservation of the tracer. Because the volume of the trace-back element is corrected in Step 2, the sum of ambient and tracer mass is conserved, and so the overall method conserves locally the mass of both fluids.

In this paper we generalize VCCMM to handle a simple model two-phase flow problem in a one-dimensional porous medium by defining a fully locally conservative Eulerian-Lagrangian tracer method. Compared to the linear case, there are many difficulties associated with the nonlinear two-phase problem. First, tracers and characteristic traces are not the same curves. Normally one traces characteristics, since these are straight lines (at least until characteristics collide). However, in our method, we transport mass over a time step, so we must follow the tracers of the flow, since these are the particle paths [25, 16]. Thus, we do *not* follow characteristics. The second complication is that the saturation changes along the tracers, which therefore follow nonlinear trajectories. Third, the tracers of the two phases differ. Fourth, shocks and rarefactions may form. Finally, and most importantly, it is not possible to trace an individual tracer independent of knowledge of the nearby saturation through time (see (3.3)–(3.5)), unlike characteristic tracing. As we will see, we achieve approximate tracing along individual tracers using both of the local mass conservation principles and self-consistency of the saturation values.

The method developed here is designed with more complex systems in mind than those considered in this paper. For the simple two-phase problem in one dimension, classical methods that eliminate an unknown and solve a single conservation law can obviously be more efficient. However, this advantage is restricted to model problems and cannot be extended to systems such as compositional petroleum reservoir models.

Our formulation does not depend on any special properties of the model problems.

In the next section we define the two-phase flow problem as it arises in flow in porous media and abstract it to the model two-phase problem we consider. In sections 3–4, we discuss tracing along tracers and the two local mass constraints. Our new method is defined in section 5, and numerical results are presented in section 6, including some comparisons to a fifth-order central weighted essentially nonoscillatory (CWENO) scheme. Our new tracer method performs well on problems with shocks and rarefactions, and it does so on very coarse spatial grids and with time steps larger than the CFL limit. We close the paper with some conclusions in the last section.

**2. The two-phase flow problem.** For simplicity, we assume that the flow is incompressible; this is not essential for our new method. With  $s(x, t)$  the saturation of the wetting fluid, we have that [5, 21, 8]

$$(2.1) \quad \phi s_t + u_{w,x} = q_w \quad \text{and} \quad -\phi s_t + u_{nw,x} = q_{nw},$$

where subscript  $t$  or  $x$  is partial differentiation with respect to time or space, respectively,  $\phi(x)$  is the porosity,  $u_\alpha$  is the phase velocity for the wetting fluid ( $\alpha = w$ ) or the nonwetting fluid ( $\alpha = nw$ ), and  $q_\alpha(x, t, s)$  models the wells. Darcy's law governs the phase velocity and pressure  $p_\alpha$ , so, ignoring gravity,

$$(2.2) \quad u_\alpha = -\lambda_\alpha k p_{\alpha,x}, \quad \alpha = w, nw,$$

where  $k(x)$  is the (absolute) permeability, and  $\lambda_\alpha(s)$  is the phase *mobility*, i.e., relative permeability divided by the phase viscosity. The capillary pressure relation

$$(2.3) \quad p_c(s) = p_{nw} - p_w$$

completes the description of the overall system of equations. This is a system of two nearly hyperbolic flow equations.

By a rearrangement of (2.1)–(2.3), we can separate it into two systems, one elliptic and one nearly hyperbolic. With the *total velocity*  $u = u_w + u_{nw}$  and total mobility  $\lambda = \lambda_w + \lambda_{nw}$ , the *pressure equation* is

$$(2.4) \quad u_x = q \equiv q_w + q_{nw},$$

$$(2.5) \quad u = -k[\lambda_w p_{w,x} + \lambda_{nw} p_{nw,x}] = -k[\lambda p_{w,x} + \lambda_{nw} p_{c,x}] = -k[\lambda p_{nw,x} - \lambda_w p_{c,x}],$$

and the *saturation equation* is one of the two equations in (2.1). If we choose the first, for the wetting fluid, we obtain

$$(2.6) \quad \phi s_t + f(s)_x = q_w,$$

where the wetting *flux function* is

$$(2.7) \quad f(s, x) = u_w = \frac{\lambda_w}{\lambda} u + k \frac{\lambda_w \lambda_{nw}}{\lambda} p_{c,x}.$$

However, we could equivalently choose the second equation in (2.1), for the nonwetting fluid, which is

$$(2.8) \quad \phi(1-s)_t + F(1-s)_x = q_{nw},$$

with

$$(2.9) \quad F(1-s, x) = u_{nw} = \frac{\lambda_{nw}}{\lambda} u - k \frac{\lambda_w \lambda_{nw}}{\lambda} p_{c,x}.$$

We now describe the model problem considered in this paper, which is fairly commonly used to describe two-phase flow in the petroleum literature [21, 20, 8]. We assume appropriate boundary conditions so that we can take  $q = q_w = q_{nw} = 0$ , and then  $u$  is a known constant solved from (2.4). We also assume that  $\phi \equiv 1$  and the flux functions depend explicitly only on  $s$ , i.e., not on  $x$  (or  $t$ ). Thus, in terms of the nonwetting saturation  $z$ ,

$$(2.10) \quad s_t + f(s)_x = 0,$$

$$(2.11) \quad z_t + F(z)_x = 0,$$

$$(2.12) \quad s + z = 1,$$

$$(2.13) \quad f(s) + F(z) = u.$$

Since  $u$  is known, this system is redundant, and only one of (2.10) and (2.11) is needed. However, we will use both equations numerically, for the reasons outlined in section 1. For simplicity, we will assume that the phases travel to the right. That is, we assume that each of  $f$ ,  $f'$ ,  $F$ , and  $F'$  is nonnegative. This is not essential to the method; countercurrent flow, in which the two phases move in opposite directions, could be treated. If the domain of interest is  $(0, 1)$ , we require the following boundary and initial conditions:

$$(2.14) \quad s(0, t) = s_B(t) \quad (\text{and } z(0, t) = z_B(t) = 1 - s_B(t)),$$

$$(2.15) \quad s(x, 0) = s^0(x) \quad (\text{and } z(x, 0) = z^0(x) = 1 - s^0(x)),$$

where  $0 \leq s_B(t) \leq 1$  and  $0 \leq s^0(x) \leq 1$ .

**3. Tracelines.** Suppose we have a sequence of time levels  $0 = t^0 < t^1 < \dots < t^N$  at which we wish to compute the solution. In one time step  $t^n$  to  $t^{n+1}$ , the characteristic lines of (2.10) describe the curves (i.e., lines) on which the saturation is constant. The characteristic trace-back  $\tilde{x}_c(t) = \tilde{x}_c(x; t) = \tilde{x}_c^{n+1}(x, t)$  passing through  $(x, t^{n+1})$  satisfies the differential equation

$$(3.1) \quad \frac{d\tilde{x}_c}{dt} = f'(s(\tilde{x}_c, t)), \quad t^n \leq t \leq t^{n+1},$$

$$(3.2) \quad \tilde{x}_c(t^{n+1}) = x.$$

Since the saturation is constant along each characteristic, individual curves can be traced trivially as straight lines, and the only complication occurs at rarefactions and shocks, where characteristics rarefy or collide. Moreover, since the saturation is constant, both the wetting and nonwetting fluids have the same characteristics.

The wetting tracelines  $\tilde{x}_w(x; t)$  satisfy a more difficult differential equation (see [13, 25, 16] or section 4), although the advantage is that tracelines fill space and do not cross each other (they move physical mass, hence are always well defined; the particle velocity does not depend explicitly on  $f'$ ). In this paper, we work only on the interval  $(t^n, t^{n+1})$  and trace backward in time (at least until we reach the boundary  $x = 0$ ), so we have that

$$(3.3) \quad \frac{d\tilde{x}_w}{dt} = \frac{f(s(\tilde{x}_w, t))}{s(\tilde{x}_w, t)}, \quad t^n \leq t \leq t^{n+1},$$

$$(3.4) \quad \tilde{x}_w(x; t^{n+1}) = x,$$

on which the saturation  $\check{s}_w(t) = \check{s}_w(x; t) = s(\check{x}_w(x; t), t)$  changes as

$$(3.5) \quad \frac{d\check{s}_w}{dt} = s_x(\check{x}_w, t) \frac{d\check{x}_w}{dt} + s_t(\check{x}_w, t) = s_x(\check{x}_w, t) \left( \frac{f(\check{s}_w)}{\check{s}_w} - f'(\check{s}_w) \right),$$

using (3.3) and (2.10). Similarly, the nonwetting tracers satisfy

$$(3.6) \quad \frac{d\check{x}_{nw}}{dt} = \frac{F(z(\check{x}_{nw}, t))}{z(\check{x}_{nw}, t)}, \quad t^n \leq t \leq t^{n+1},$$

$$(3.7) \quad \check{x}_{nw}(x; t^{n+1}) = x,$$

on which the saturation  $\check{z}_{nw}(t) = z(\check{x}_{nw}(x; t), t)$  changes as

$$(3.8) \quad \frac{d\check{z}_{nw}}{dt} = z_x(\check{x}_{nw}, t) \left( \frac{F(\check{z}_{nw})}{\check{z}_{nw}} - F'(\check{z}_{nw}) \right).$$

Note that (3.5) and (3.8) imply that individual tracers cannot be traced independently of knowledge of the solution in a neighborhood of the tracer itself. That is, we require knowledge of the space (or, equivalently, time) derivative of the saturation.

**4. Local mass constraints.** Let the domain  $(0, 1)$  be partitioned by grid points  $0 = x_0 < x_1 < \dots < x_N = 1$  into elements (i.e., subintervals)  $\mathcal{T} = \{E_i = (x_{i-1}, x_i) : i = 1, 2, \dots, N\}$ . Let  $E \in \mathcal{T}$  be an element, and define the space-time trace-back region of  $E$  from time  $t^{n+1}$  back to  $t^n$  as

$$\mathcal{E}_{E,w} = \{(\check{x}, t) \in (0, 1) \times [t^n, t^{n+1}] : \check{x} = \check{x}_w(x, t) \text{ for some } x \in E\}.$$

Orienting ourselves with time advancing upwards, the “top” of the region is  $E$ , the “bottom” is the trace-back region

$$(4.1) \quad \check{E}_w = \{\check{x} \in (0, 1) : \check{x} = \check{x}_w(x, t^n) \text{ for } x \in E\} = \mathcal{E}_{E,w} \cap \{t^n\},$$

and the “side”

$$\mathcal{S}_{E,w} = \{(\check{x}, t) \in \partial\mathcal{E}_{E,w} : \check{x} = \check{x}_w(x; t) \text{ for } x \in \partial E\}$$

is the space boundary of the space-time region  $\mathcal{E}_{E,w}$ .

Notice that (2.10) can be rewritten as the space-time divergence

$$(4.2) \quad \nabla_{t,x} \cdot \begin{pmatrix} s \\ f(s) \end{pmatrix} = 0.$$

Applying the divergence theorem gives

$$(4.3) \quad \int_{\partial\mathcal{E}_{E,w}} \begin{pmatrix} s \\ f(s) \end{pmatrix} \cdot \nu_{t,x} d\sigma = \int_{\mathcal{S}_{E,w}} \begin{pmatrix} s \\ f(s) \end{pmatrix} \cdot \nu_{t,x} d\sigma + \int_E s^{n+1} dx - \int_{\check{E}_w} s^n dx = 0,$$

where  $\nu_{t,x}$  is the unit outward normal vector to  $\partial\mathcal{E}_{E,w}$  and we use the superscript  $n$  to denote a time-dependent function evaluated at time  $t^n$ . The tracer traces are defined precisely by (3.3) so that

$$(4.4) \quad \begin{pmatrix} s \\ f(s) \end{pmatrix} \cdot \nu_{t,x} = 0,$$

at least when the tracers are within the domain  $(0, 1)$ . Thus when  $E = E_i = (x_{i-1}, x_i)$ , the *local wetting mass constraint* is

$$(4.5) \quad \int_{E_i} s^{n+1} dx = \int_{\check{E}_{i,w}} s^n dx + \int_{t_{w,i}^n}^{t_{w,i-1}^n} f(s_B) dt,$$

where  $t_{w,j}^n = t^n$  unless the tracer from  $x_j$  traces to  $x = 0$ , in which case  $t_{w,j}^n$  is the greatest time at which this occurs. Similarly, we have the *local nonwetting mass constraint*

$$(4.6) \quad \int_{E_i} z^{n+1} dx = \int_{\check{E}_{i,nw}} z^n dx + \int_{t_{nw,i}^n}^{t_{nw,i-1}^n} F(z_B) dt.$$

The sum of the two gives what we call the *local volume constraint*

$$(4.7) \quad |E_i| = \int_{\check{E}_{i,w}} s^n dx + \int_{\check{E}_{i,nw}} z^n dx + \int_{t_{w,i}^n}^{t_{w,i-1}^n} f(s_B) dt + \int_{t_{nw,i}^n}^{t_{nw,i-1}^n} F(z_B) dt,$$

where  $|E_i| = x_i - x_{i-1}$  is the length of the interval. The Eulerian-Lagrangian tracer method is defined by (4.5) once we define the tracer trace-back regions  $\check{E}_w$  as in (4.1).

**5. The numerical method.** We present our tracer method in this section.

Since there is no physical reason to prefer one fluid over the other, we require that the numerical method is in no way biased toward either the wetting or nonwetting fluid, as motivated in section 1. Such a bias can hide difficulties that will emerge in more complicated problems. For instance, in the classical Buckley-Leverett problem considered in section 6, the nonwetting tracers are substantially less smooth than the wetting tracers. Methods that eliminate an unknown and solve only for the wetting saturation will have an advantage in the model problem, but will have to deal with the nonwetting-phase behavior in more general situations.

We approximate the saturation  $s$  in three different ways. First, we assume that  $s$  is a piecewise discontinuous constant in each grid element of the partition  $\mathcal{T}$ . We use the notation  $s_E^n$  and  $z_E^n = 1 - s_E^n$  for the constant approximate average wetting and nonwetting saturations in the element  $E \in \mathcal{T}$  at time  $t^n$ . The method—see (5.3)—will set these piecewise constants in a locally mass conservative way (i.e., according to (4.5)).

However, to trace backward in time the boundary of each element  $E = (x_i, x_{i+1}) \in \mathcal{T}$ , we will need an approximation to the saturation  $s$  at the grid points. Therefore, our second approximation of the saturation will be to compute pointwise approximations  $s_i$  to  $s(x_i)$  for each grid point  $x_i$ . These saturations will not satisfy the local mass constraint, and so can be viewed as auxiliary approximations that are not otherwise used.

Finally, our third and last approximation of  $s$  is given by postprocessing the average element saturations  $s_E$ , using the grid saturations  $s_i$ , to improve our overall approximation. The postprocessed saturation  $\tilde{s}(x)$  is piecewise discontinuous linear. Since it is locally mass conservative over the grid and higher order, it should be considered our final and most accurate approximation of the saturation function  $s(x)$ . We describe this postprocessing step next.

**5.1. Saturation postprocessing.** It is a standard practice to postprocess a piecewise constant approximation to construct a piecewise discontinuous linear polynomial in each grid element of the partition  $\mathcal{T}$ . It must be appropriately slope-limited to avoid local extrema and maintain saturations between 0 and 1. The result is a higher order approximation away from shocks (see, e.g., [6, 4]). We present the post-processing we use; however, there are many choices, since these techniques are fairly well established and many slope limiters are available.

Our postprocessing is local. On  $E = (x_{i-1}, x_i) \in \mathcal{T}$ , we are given the element saturation  $s_E^n$  and saturations  $s_{i-1}^n$  and  $s_i^n$  at the grid points  $x_{i-1}$  and  $x_i$ , respectively. We define our piecewise discontinuous linear function  $\tilde{s}^n(x)$  such that the average mass over each element remains fixed and the function tilts to the grid value requiring the least slope (in absolute value), unless a local extremum would result, in which case a zero slope is assumed. That is, on  $E$ , we define the slopes

$$\sigma_{i-1}^n = \frac{s_E^n - s_{i-1}^n}{\frac{1}{2}(x_i - x_{i-1})} \quad \text{and} \quad \sigma_i^n = \frac{s_i^n - s_E^n}{\frac{1}{2}(x_i - x_{i-1})},$$

$$\sigma_E^n = \begin{cases} 0 & \text{if } \sigma_{i-1}^n \text{ and } \sigma_i^n \text{ have opposite signs,} \\ \sigma_{i-1}^n & \text{if not the case above and } |\sigma_{i-1}^n| \leq |\sigma_i^n|, \\ \sigma_i^n & \text{otherwise,} \end{cases}$$

and then

$$(5.1) \quad s(x, t^n) \approx \tilde{s}^n(x) = s_E^n + \sigma_E^n \left( x - \frac{1}{2}(x_i + x_{i-1}) \right) \quad \text{for } x \in E.$$

Trivially we define  $z_E^n = 1 - s_E^n$  and  $\tilde{z}^n = 1 - \tilde{s}^n$  for any  $n$  and  $E$ . Note that the definitions could instead be stated equivalently for the nonwetting fluid, defining  $\tilde{z}^n$  similar to the construction above and then defining  $\tilde{s}^n = 1 - \tilde{z}^n$ . That is, there is no bias to the wetting fluid in this postprocessing step.

**5.2. Time-step advance.** Initially we define for all  $E \in \mathcal{T}_h$

$$(5.2) \quad s_E^0 = \frac{1}{|E|} \int_E s^0(x) dx$$

and postprocess using the values  $s^0(x_i)$  to obtain  $\tilde{s}^0(x)$ . It is simple to advance in time from  $t^n$  to  $t^{n+1}$  on  $E = E_i \in \mathcal{T}_h$  using the local mass constraint (4.5) as

$$(5.3) \quad |E_i| s_{E_i}^{n+1} = \int_{\tilde{E}_{i,w}} \tilde{s}^n dx + \int_{t_{w,i}^n}^{t_{w,i-1}^n} f(s_B) dt$$

$$= \sum_{F \in \mathcal{T}} \int_{\tilde{E}_{i,w} \cap F} \tilde{s}^n dx + \int_{t_{w,i}^n}^{t_{w,i-1}^n} f(s_B) dt.$$

It remains to determine  $\tilde{E}_{i,w}$ , perhaps  $t_{w,i-1}^n$  and  $t_{w,i}^n$ , and the grid saturations for the postprocessing step. This will complete the definition of the numerical method.

We use the notation  $\tilde{x}_{w,i}(t) = \tilde{x}_w(x_i; t)$ . We begin with  $x = x_0 = 0$ , which, by our assumptions on the flow direction, immediately traces out of the domain. Thus

$$(5.4) \quad \tilde{x}_{w,0}^n = \tilde{x}_{nw,0}^n = 0 \quad \text{and} \quad t_{w,0}^n = t_{nw,0}^n = t^{n+1} \quad \text{for all } n.$$

We work sequentially to define  $\tilde{x}_{w,i}^n$  and  $\tilde{x}_{nw,i}^n$ , and possibly  $t_{w,i}^n$  and/or  $t_{nw,i}^n$ , for  $i = 1, 2, \dots, N$ . Then  $\tilde{E}_{w,i} = (\tilde{x}_{w,i-1}^n, \tilde{x}_{w,i}^n)$  and  $\tilde{E}_{nw,i} = (\tilde{x}_{nw,i-1}^n, \tilde{x}_{nw,i}^n)$ .

**5.3. Numerical tracing along tracers.** Exact tracing of the tracers defined by (3.3)–(3.5) is not possible, as noted in section 3. We will therefore solve a local minimization problem to find each needed trace-back point  $\tilde{x}_w(x, t^n)$ . The minimization problem is given in the next subsection (see (5.13)) and it will be subject to the constraints of mass conservation, which is a strong constraint on the numerics. For each fixed grid point  $x = x_i$ , we will set up a function  $\mathcal{F}(s_g, \delta)$  of two parameters, which are guesses of the wetting saturation  $s_g$  at  $x$  (a grid point) and its space derivative  $\delta = s_x$  at the advanced time  $t^{n+1}$ . In terms of these two parameters, we can trace (approximately) from time  $t^{n+1}$  both the point and the (grid) saturation backward in time to  $t^n$  along the tracer. The function  $\mathcal{F}$  will measure the discrepancy between the saturation found through tracing backward in time and the saturation previously computed by the method up to the time  $t^n$ . These two should agree if we have consistency within the method.

In this subsection, we describe the tracing of the fixed grid point  $x = x_i$  back to  $\tilde{x}_w(x, t^n)$ , assuming  $s_g$  and  $\delta$  are given. To simplify notation, we drop the subscript  $i$  from the following tracing description. We simplify the computational effort by using a Taylor approximation for  $\tilde{x}_w(x; t)$ . Clearly, a simple Taylor approximation to the tracer itself would be inadequate, especially near shocks. However, we do not need the entire trajectory of the tracer, but only its trace-back position  $\tilde{x}_w(x, t^n)$ , which is determined by the two parameters  $s_g$  and  $\delta$ . In the next subsection we determine the correct choices of these parameters so as to satisfy the local mass conservation principles and self-consistency. These physical principles, and not the Taylor approximation, determine the location of the trace-back points  $\tilde{x}_w(x, t^n)$ . The numerical results of section 6 will show the adequacy of our approximate tracing procedure.

The first derivative of  $\tilde{x}_w$  is given by (3.3), and so the second derivative is

$$\frac{d^2 \tilde{x}_w^{n+1}}{dt^2} = \frac{1}{s_g} \left( f'(s_g) - \frac{f(s_g)}{s_g} \right) \frac{d s_w^{n+1}}{dt} = -\frac{1}{s_g} \left( \frac{f(s_g)}{s_g} - f'(s_g) \right)^2 s_x^{n+1},$$

using (3.5). With  $\Delta t = t^{n+1} - t^n$ , we have that

$$(5.5) \quad \begin{aligned} \tilde{x}_w = \tilde{x}_w(x; t^n) &\approx x - \frac{d \tilde{x}_w^{n+1}}{dt} \Delta t + \frac{1}{2} \frac{d^2 \tilde{x}_w^{n+1}}{dt^2} \Delta t^2 \\ &\approx x - \frac{f(s_g)}{s_g} \Delta t - \frac{1}{2 s_g} \left( \frac{f(s_g)}{s_g} - f'(s_g) \right)^2 \delta \Delta t^2. \end{aligned}$$

If we determine that  $\tilde{x}_w < 0$ , we set  $\tilde{x}_w = 0$  and define the time of exit  $t_w^n$  from

$$(5.6) \quad 0 = x - \frac{f(s_g)}{s_g} (t^{n+1} - t_w^n) - \frac{1}{2 s_g} \left( \frac{f(s_g)}{s_g} - f'(s_g) \right)^2 \delta (t^{n+1} - t_w^n)^2;$$

otherwise,  $t_w^n = t^n$ .

The nonwetting fluid is similar. The values of nonwetting saturation  $z_g = 1 - s_g$  and spatial slope  $-\delta$  follow from (2.12). The Taylor approximation is therefore

$$(5.7) \quad \tilde{x}_{nw} = \tilde{x}_{nw}(x; t^n) \approx x - \frac{F(z_g)}{z_g} \Delta t + \frac{1}{2 z_g} \left( \frac{F(z_g)}{z_g} - F'(z_g) \right)^2 \delta \Delta t^2,$$

with  $t_{nw}^n = t^n$ , unless  $\tilde{x}_{nw} < 0$ , in which case we set  $\tilde{x}_{nw} = 0$  and define the time of exit  $t_{nw}^n$  from

$$(5.8) \quad 0 = x - \frac{F(z_g)}{z_g} (t^{n+1} - t_{nw}^n) + \frac{1}{2 z_g} \left( \frac{F(z_g)}{z_g} - F'(z_g) \right)^2 \delta (t^{n+1} - t_{nw}^n)^2.$$

We approximate the wetting saturation at the trace-back point  $(\check{x}_w, t^n)$  by another Taylor approximation

$$(5.9) \quad \check{s}_g^n = s_g - \left( \frac{f(s_g)}{s_g} - f'(s_g) \right) \delta (t^{n+1} - t_w^n),$$

using (3.5). Similarly, at  $(\check{x}_{nw}, t^n)$ ,

$$(5.10) \quad \check{z}_g^n = z_g + \left( \frac{F(z_g)}{z_g} - F'(z_g) \right) \delta (t^{n+1} - t_{nw}^n).$$

**5.4. The volume constraint and consistency.** As stated above, without the correction step of this subsection, the use of the local wetting mass constraint in (5.3) is biased to the wetting phase. By definition, the wetting fluid is locally conserved; however, the nonwetting fluid most likely is not locally conserved. That is,

$$(5.11) \quad |E_i| z_{\check{E}_i}^{n+1} = |E_i| (1 - s_{\check{E}_i}^{n+1}) \stackrel{?}{=} \int_{\check{E}_{i,nw}} \check{z}^n dx + \int_{t_{nw,i}^n}^{t_{nw,i-1}^n} F(z_B) dt$$

most likely does not hold for every element  $E_i \in \mathcal{T}_h$ . In fact, it holds if and only if the local volume constraint (4.7) is satisfied by the numerical solution:

$$(5.12) \quad |E_i| = \int_{\check{E}_{i,w}} \check{s}^n dx + \int_{\check{E}_{i,nw}} \check{z}^n dx + \int_{t_{w,i}^n}^{t_{w,i-1}^n} f(s_B) dt + \int_{t_{nw,i}^n}^{t_{nw,i-1}^n} F(z_B) dt.$$

Since we must not bias the method to prefer one fluid over the other, we require that the numerical local volume constraint be satisfied. This will improve the overall approximation of the system, and in particular the trace-back points, by finding the best choice for  $s_g$  and  $\check{x}_w^n$  and  $\check{x}_{nw}^n$ .

We correct our approximate tracings (i.e., determine  $(s_g, \delta)$ ) so as to satisfy (5.12). However, there is an ambiguity: a larger  $\check{E}_w$  can be paired with a smaller  $\check{E}_{nw}$ , maintaining the constraint. Thus we also impose a consistency condition for each grid point  $x = x_i$ . On the one hand, starting at time  $t^{n+1}$  from our guess of the grid saturation  $s_g$  and slope  $\delta$ ,  $s_g$  evolves back in time directly according to (3.5), approximated by (5.9), to give the saturation value  $\check{s}_g^n$ . On the other hand,  $x = x_i$  itself traces back from time  $t^{n+1}$  to  $t^n$  to the point  $\check{x}_w$ , where we know the previous saturation, namely  $\check{s}^n(\check{x}_w)$ . These two saturations should agree, and give us a consistency condition that should be met, at least approximately. There is also a similar consistency for the other phase.

We solve the following minimization problem. We seek  $(s_g, \delta)$  to minimize

$$(5.13) \quad \mathcal{F}(s_g, \delta) = (\check{s}^n(\check{x}_w) - \check{s}_g^n)^2 + (\check{z}^n(\check{x}_{nw}) - \check{z}_g^n)^2$$

subject to the volume constraint (5.12) and the range constraint

$$(5.14) \quad 0 \leq s_g \leq 1.$$

Recall that  $\check{s}^n$  and  $\check{z}^n$  are known from the previous time step or initial condition; moreover, from the previous element, we have the traces  $\check{x}_{w,i-1}$  and  $\check{x}_{nw,i-1}$  (these are 0 for the first element,  $i = 1$ ). Thus we define  $\check{x}_{w,i}^n(s_g, \delta)$ ,  $\check{x}_{nw,i}^n(s_g, \delta)$ ,  $t_{w,i}^n(s_g, \delta)$ , and  $t_{nw,i}^n(s_g, \delta)$  from (5.5)–(5.8),  $\check{E}_w = (\check{x}_{w,i-1}, \check{x}_w)$ ,  $\check{E}_{nw} = (\check{x}_{nw,i-1}, \check{x}_{nw})$ , and  $\check{s}_g^n$  and  $\check{z}_g^n$  come from (5.9)–(5.10).

Once the minimization problem is solved, so that  $\tilde{x}_{w,i}^n$ ,  $\tilde{x}_{nw,i}^n$ ,  $t_{w,i}^n$ ,  $t_{nw,i}^n$ ,  $s_{g,i}^{n+1}$ , and  $\delta_i^{n+1}$  are known, we advance the wetting saturation using (5.3), which is equivalent to advancing the nonwetting saturation by (5.11), so the method is unbiased. Finally, we have the grid saturations  $s_{g,i-1}^{n+1}$  from the previous element (or the boundary value  $s_B$ ) and  $s_{g,i}^{n+1}$ , allowing us to postprocess the piecewise constant solution to form  $\tilde{s}^{n+1}$  and  $\tilde{z}^{n+1}$ . The description of the method is complete.

As shown through the numerical results of the next section, the proposed method gives an accurate solution even in the presence of shocks. This may be expected in regions where the solution is smooth, since the Taylor approximations used in defining the method should give an accurate approximation of the entire traceline (5.5) and trace-back saturation (5.9). Near an isolated shock, however, the traceline is continuous, but it has a slope discontinuity. Even though the Taylor approximated traceline is inaccurate, the trace-back points  $\tilde{x}_w^n$  and  $\tilde{x}_{nw}^n$  can still be approximated accurately by a careful choice of the parameters  $s_g$  and  $\delta$ , which are set to respect the physics by solving the minimization problem (5.13). In fact, the method can handle nonisolated shocks as well, as Example 8 of the numerical results will show.

In practice, we find it helpful to also constrain  $\delta$  to some reasonable range:

$$(5.15) \quad \delta_{\min} \leq \delta \leq \delta_{\max}.$$

This modification allows us to more easily and robustly solve the minimization problem. We may continue to allow  $\delta$  to vary freely by taking extremely liberal limits. Moreover, monotonicity can be achieved by using the previous grid point's  $\delta$  value as one bound for  $\delta$  at the current grid point (e.g., if it is known that the saturation is convex or concave).

We close this section with a brief remark on a possible modification to the minimization procedure (5.13). At first glance, it might seem prudent to try to detect if we are at a shock by, for example, noting when  $s$  changes rapidly and  $|\delta|$  is very large. In this case, instead of tracing along the traceline using (5.5) and (5.7), we might instead trace at the Rankine-Hugoniot shock speed [20]; that is, in essence, we may trace the characteristic (3.1) rather than the traceline, using the fixed shock saturation value. Although this seems like a reasonable strategy, we found that it was unnecessary. We obtained good results without adding this extra knowledge of the shock. In fact, all of our numerical results to be given in the next section, except the first, use neither analytic knowledge of the shock structure nor any explicit shock detection strategy.

**6. Some numerical results.** In our examples, we plot the wetting saturation. However, since the method treats both phases identically, every numerical example actually computes two results. That is, a numerical example of the wetting phase saturation  $s$ , using flux function  $f$ , initial condition  $s^0$ , and boundary condition  $s_B$ , will also cover the numerical example for  $z = 1 - s$ , using flux function  $F = u - f$ , initial condition  $z^0 = 1 - s^0$ , and boundary condition  $z_B = 1 - s_B$ . One need simply consider the plot of  $1 - s$ . So, for example, shock propagation with the left state  $s_L$  greater than the right state  $s_R$  also demonstrates the case of shock propagation with the state magnitudes reversed. Similarly, a convex flux function example in which  $f'' > 0$  is paired to a concave example with  $F'' = -f'' < 0$ .

We also compare our numerical results with the fifth-order CWENO (CWENO-5) scheme [23]. The CWENO-5 results were obtained from a code provided by the Computational Fluid Dynamics Laboratory [9]. We used the publicly available software package FFSQP [19, 31] to solve our minimization problem.

**6.1. The Buckley–Leverett equation.** We begin with four test examples involving the classic Buckley–Leverett problem, defined by

$$(6.1) \quad s_t + f(s)_x = 0, \quad x \in (0, 1), t \in (0, 1),$$

$$(6.2) \quad z_t + F(z)_x = 0, \quad x \in (0, 1), t \in (0, 1),$$

where  $s + z = 1$  and the wetting fractional flow is

$$(6.3) \quad f(s) = \frac{s^2}{s^2 + (1-s)^2}.$$

The nonwetting fractional flow is  $F(z) = u - f(s)$ , where  $u$  is the constant total velocity of the system. Since “particles” at zero saturation should have zero velocity (or, equivalently, traceline velocities  $F(z)/z$  should remain bounded as  $z \rightarrow 0$ ), we require that  $u = f(1) = 1$  in this case. Thus

$$(6.4) \quad F(z) = 1 - f(1-z) = \frac{z^2}{z^2 + (1-z)^2}.$$

These flux functions are neither convex nor concave (they are S-shaped).

The maximal characteristic speed is  $f'(0.5) = 2$ , so, in general, the CFL time step limit for a uniform grid of spacing  $h$  using time step  $\Delta t$  is  $\Delta t \leq h/2$ .

**6.1.1. Example 1.** In the first numerical example, we assume the Buckley–Leverett problem with initial and boundary conditions

$$(6.5) \quad s(x, 0) = s^0(x) = 0 \quad \text{and} \quad s(0, t) = 1.$$

Initially, this is a pure shock; however, in time the solution also develops a rarefaction behind the shock. The shock occurs when the characteristic and traceline velocities agree; that is, when

$$f'(s_{\text{shock}}) = \frac{f(s_{\text{shock}})}{s_{\text{shock}}},$$

which gives  $s_{\text{shock}} = 1/\sqrt{2} = 0.7071$  as the saturation at the (trailing edge of the) shock. The Rankine–Hugoniot condition implies a shock speed of

$$u_{\text{shock}} = \frac{f(s_{\text{shock}}) - f(0)}{s_{\text{shock}} - 0} = 1.2071.$$

The CFL limit for this particular problem is a little better than the general case, and it is given by

$$\Delta t_{\text{CFL}} = \frac{h}{1.2071}.$$

Since we are merely testing the method, in this example, we will use our analytic knowledge of the shock position for all time. Moreover, we trace points back in time according to (5.5) only until we hit the shock. That is, for those points that trace into the shock, we trace from time  $t^{n+1}$  back only to time  $\tilde{t} > t^n$ , until we advance to the shock position, and then assume the saturation changes discontinuously at the shock appropriately. We then trace using the true saturation and arrive at the previous time  $t^n$ .

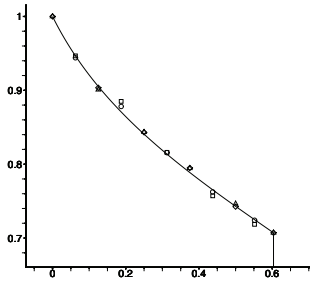


FIG. 6.1. Ex. 1. The exact solution at time 0.5 is the solid line, and the approximate solution values are shown using 8 elements ( $h = 1/8$ ) and  $\Delta t = 1/4$ , which is 2.4 times the CFL limit. The open squares and circles give the average saturation in the element (plotted at the element center) with  $\delta$  unbounded and constrained to be increasing, respectively. The open diamonds and triangles give the grid values with  $\delta$  unbounded and constrained to be increasing, respectively.

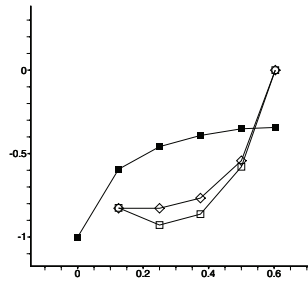


FIG. 6.2. Ex. 1. The actual values of  $s_x$  in solid squares versus the values of  $\delta$  actually computed in open symbols. The diamond symbols show results with  $\delta$  constrained to be increasing; square symbols are used for unbounded  $\delta$ .

In Figure 6.1, we show the results at time  $t = 0.5$  on a uniform grid of 8 elements ( $h = 1/8$ ). We use a time step  $\Delta t = 2h = 1/4$ , which is 2.4 times the CFL time step. The red curve is the true solution. The green symbols give the grid values that we compute in the algorithm, while the solution itself (the average saturation in the element, plotted at the element center) is shown in blue. Two results are shown. The diamond symbols show results with  $\delta$  being constrained to be increasing (see (5.15)), while square symbols are used for the results allowing unbounded  $\delta$ . In Figure 6.2, we plot the computed  $\delta$  values and the true  $s_x$  values at the grid points.

As the results show, we have correctly approximated the rarefaction. Moreover, we have done so on an extremely coarse mesh: by time 0.5, we have used only five points to resolve the rarefaction. The computed values of  $\delta$  are also in line with the correct values.

We have used analytic knowledge of the shock structure in this first example. In each of our remaining examples, we will not use any such information (e.g., we will not assume the shock position, speed, or saturation). Instead we will let the method, with its use of both local mass conservation principles and self-consistency, determine the shock and rarefaction structures by itself. As we will note, our only input will be in the constraints used in the minimization problem, i.e., in (5.14)–(5.15).

**6.1.2. Example 2.** This example is identical to Example 1, except that no shock information is assumed in the computation. For our new scheme, we use  $h = 1/25$  and  $\Delta t = 1/42$ , and we compare to CWENO-5 using a finer grid  $h = 1/40$  and  $\Delta t = 1/240$ , which is 0.2 times the general CFL time step. Our time step is 5.7 times larger than that used by the CWENO-5 scheme.

The results at time  $t = 0.5$  are given in Figure 6.3. Compared to CWENO-5, our scheme better follows the rarefaction up to right before the shock, and better captures the right foot of the shock. However, it is worse than CWENO-5 near and to the left of the shock; some oversmoothing is observed.

**6.1.3. Example 3.** In this example, we show shock formation. We base the initial condition on the true solution of the previous Buckley–Leverett problem at

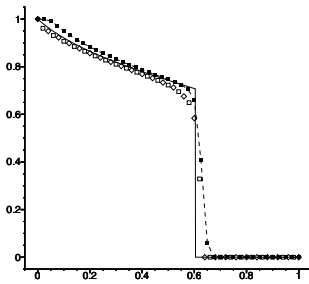


FIG. 6.3. Ex. 2. The exact solution at time 0.5 is the solid line, and the approximate solution values are shown using 25 elements ( $h = 1/25$ ) and  $\Delta t = 1/42$ . The open diamonds give the grid values, and open squares give the average saturation in the element (plotted at the element center). The solid squares and black dashed line give the CWENO-5 results using  $h = 1/40$  and  $\Delta t = 1/240$ .

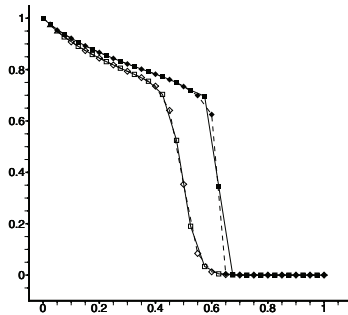


FIG. 6.4. Ex. 3. Shock formation for  $h = 1/20$  and  $\Delta t = h$ . The open symbols show the initial condition ( $t = t_0$ ), and solid symbols show the concentration at  $t = t_0 + 0.1$ , which is just before the shock has formed. Diamond symbols stand for grid values and squares for average element values.

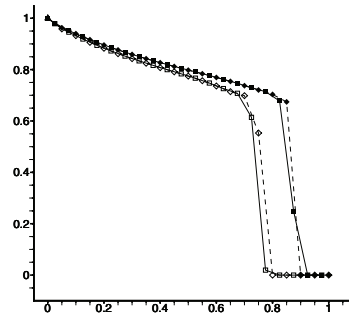


FIG. 6.5. Ex. 3. Shock formation for  $h = 1/20$  and  $\Delta t = h$ . The open and solid symbols show the concentration at  $t = t_0 + 0.2$  and  $t = t_0 + 0.3$ , respectively. Note that the shock has formed and propagates. Diamond symbols stand for grid values and squares for average element values.

time  $t = t_0 = 0.414213$ , so the shock is at  $x = 0.5$ . We take the true solution for  $x \leq 0.5$ , extend the shock saturation  $s_{\text{shock}} = 1/\sqrt{2}$  for  $x > 0.5$ , and finally multiply by the approximate Heaviside function

$$H(x) = \frac{1}{1 + \exp(40(x - 0.5))}.$$

This produces a smooth initial condition (see Figure 6.4) that relatively quickly forms a shock. We impose a monotonicity constraint on the solution at the advanced time level (see (5.14)), which on the element  $E = (x_i, x_{i+1})$  is

$$(6.6) \quad s(x_i) \leq s_E \leq s(x_{i+1}),$$

where  $s(x_i)$  and  $s(x_{i+1})$  are the grid saturation values at time  $t^{n+1}$ , and  $s(x_i)$  was computed from the previous element and  $s(x_{i+1})$  and  $s_E$  are being computed from the minimization problem for the current element  $E$ .

First, we choose  $h = 1/20$  and  $\Delta t = h = 1/20$ . We show the initial condition at time  $t = t_0$  and results at  $t = t_0 + 2\Delta t = t_0 + 0.1$  in Figure 6.4 and at  $t = t_0 + 4\Delta t = t_0 + 0.2$  and  $t = t_0 + 6\Delta t = t_0 + 0.3$  in Figure 6.5. Again, green symbols stand for grid

values, and the blue symbols for the average element concentrations. The triangles are the earlier time, and squares represent the later time. The shock is almost formed at time  $t = t_0 + 2\Delta t$ . There is only a single average element value at the jump. The shock fully forms and propagates for the later two times. This shows that our scheme is capable of handling shock formation.

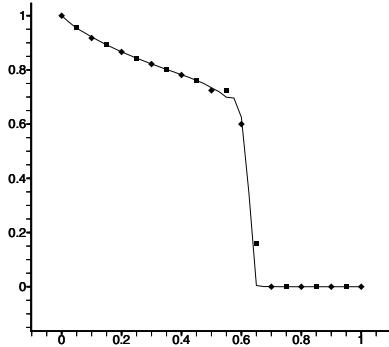


FIG. 6.6. Ex. 3. Shock formation for  $h = 1/10$  and  $\Delta t = h$ . The concentration is at  $t = t_0 + 0.1$ , with diamond symbols standing for grid values and squares for average element values. For comparison, the solid curve is obtained by linking the 20 grid values and 20 average element values from Figure 6.4 (where  $\Delta t = h = 1/20$ ).

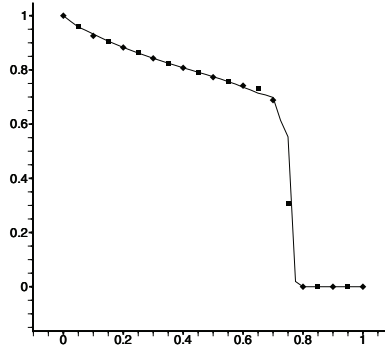


FIG. 6.7. Ex. 3. Shock formation for  $h = 1/10$  and  $\Delta t = h$ . The concentration is at  $t = t_0 + 0.2$ , with diamond symbols standing for grid values and squares for average element values. For comparison, the solid curve is obtained by linking the 20 grid values and 20 average element values from Figure 6.5 (where  $\Delta t = h = 1/20$ ).

We next show results for a bigger time step,  $\Delta t = 1/10$ , but we also coarsen the grid to  $h = 1/10$  so we maintain the same ratio  $\Delta t/h = 1$ . Our new results ( $\Delta t = 1/10$ ) are compared to our previous results ( $\Delta t = 1/20$ ) from Figures 6.4–6.5. In Figure 6.6, we show the result at time  $t = t_0 + 0.1$ , where green symbols stand for grid values and blue symbols for average element values. The red curve is obtained by linking the 20 grid values and 20 average element values from our previous results in Figure 6.4. Similarly, Figures 6.7–6.8 show results at  $t = t_0 + 0.2$  and  $t = t_0 + 0.3$ , respectively. The results show that we can attain good results on a fairly coarse grid.

Finally, we ran the test with  $h = 1/20$  and a time step much larger than the CFL limit,  $\Delta t = 2h = 1/10$ . Results are shown in Figures 6.9–6.11, at the same three times as before. In these figures, the red curves and red squares are the average element values from the first series of runs when  $\Delta t = h = 1/20$  and blue squares are our new results with  $\Delta t = 1/10$  and  $h = 1/20$ . The figures indicate that our scheme can handle relatively large time steps. We do note, however, that in this test we relaxed the monotonicity constraint (6.6) to

$$s(x_i) + \epsilon \leq s(x_{i+1/2}) \leq s(x_{i+1}) - \epsilon$$

for some small  $\epsilon > 0$  (we used  $\epsilon = 1e-4$ ). The reason is that otherwise we could not get a feasible solution to the minimization problem from the code we used. This relaxation can be seen in Figures 6.9 and 6.11 (but not in Figure 6.10), where the blue value at the shock is slightly larger than the one to its left.

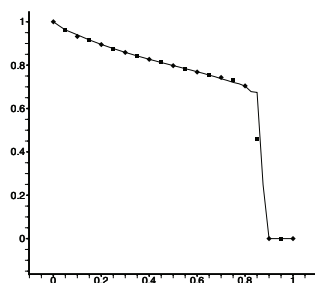


FIG. 6.8. Ex. 3. Shock formation for  $h = 1/10$  and  $\Delta t = h$ . The concentration is at  $t = t_0 + 0.3$ , with diamond symbols standing for grid values and squares for average element values. For comparison, the solid curve is obtained by linking the 20 grid values and 20 average element values from Figure 6.5 (where  $\Delta t = h = 1/20$ ).

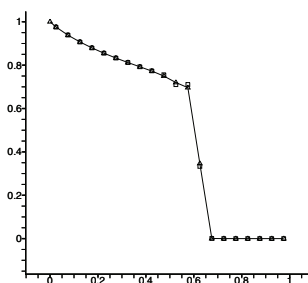


FIG. 6.9. Ex. 3. Shock formation for  $h = 1/20$  and  $\Delta t = 2h$  at  $t = t_0 + 0.1$ . The open squares show the average element concentrations. For comparison, the solid curve and open triangles are the average element values from  $\Delta t = h = 1/20$ .

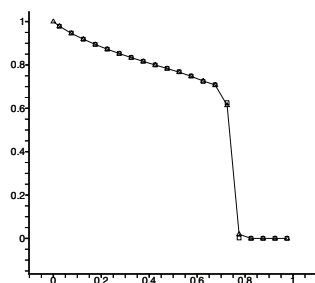


FIG. 6.10. Ex. 3. Shock formation for  $h = 1/20$  and  $\Delta t = 2h$  at  $t = t_0 + 0.2$ . The open squares show the average element concentrations. For comparison, the solid curve and open triangles are the average element values from  $\Delta t = h = 1/20$ .

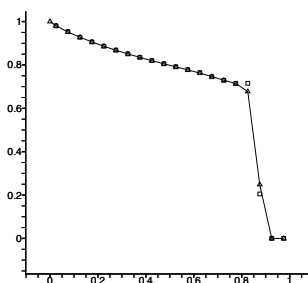


FIG. 6.11. Ex. 3. Shock formation for  $h = 1/20$  and  $\Delta t = 2h$  at  $t = t_0 + 0.3$ . The open squares show the average element concentrations. For comparison, the solid curve and open triangles are the average element values from  $\Delta t = h = 1/20$ .

**6.1.4. Example 4.** In this final example involving the Buckley–Leverett problem, we show a complex interaction of shocks and rarefactions. The initial condition

$$(6.7) \quad s^0(x) = \begin{cases} 1 - 20x & \text{for } 0 \leq x \leq 0.05, \\ 0.5 & \text{for } 0.25 \leq x \leq 0.4, \\ 0 & \text{otherwise} \end{cases}$$

represents two separated regions, each initially occupied by a pulse of the wetting fluid. Both pulses propagate to the right. The initial pulse over  $[0, 0.05]$  is sustained by the boundary condition at  $x = 0$ , and it travels faster than the other pulse at  $[0.25, 0.4]$ .

In Figure 6.12, we plot the solution at four times. The true solution (i.e., a finely discretized CWENO-5 solution with  $h = 1/1280$  and  $\Delta t = 1/15360$ ) is shown in red. Two traceline method solutions are shown. These are the average element concentrations (we do not show the grid concentration values derived by the minimization procedure in this figure). The red diamonds are the result of using  $h = 1/40 = 0.025$  and  $\Delta t = 1/80$ . The blue squares are the traceline result using  $h = 1/80 = 0.0125$  and

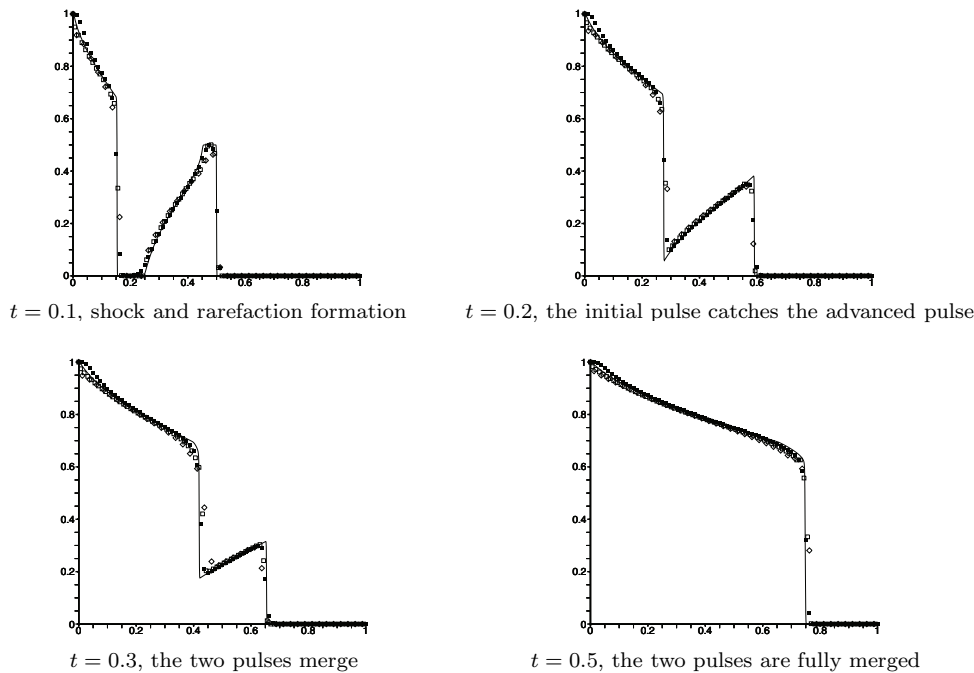


FIG. 6.12. Ex. 4. A complex Buckley–Leverett problem with the initial condition of two pulses given in (6.7). The solid line is the reference solution, given by CWENO-5 with a very small  $h = 1/1280$  and  $\Delta t = 1/15360$ . The traceline method results are shown as average element values (but no grid values), using open diamonds for  $h = 1/40$  and  $\Delta t = 1/80$ , and using open squares for  $h = 1/80$  and  $\Delta t = 1/160$ . For comparison, the solid squares are the CWENO-5 results using  $h = 1/80$  and  $\Delta t = 1/480$ .

$\Delta t = 1/160$ . For comparison, the black symbols show the CWENO-5 results using  $h = 1/80 = 0.0125$  and a much finer  $\Delta t = 1/480$ . These time steps were chosen since for larger  $\Delta t$ , CWENO-5 becomes unstable and the traceline method shows decreased accuracy.

One can see in Figure 6.12 that by  $t = 0.1$ , a shock and rarefaction has formed on the first pulse, while the second pulse has developed a trailing rarefaction. By  $t = 0.2$ , the initial pulse has caught up to the advanced pulse. At  $t = 0.3$ , the two pulses are continuing to merge. The traceline method solution is a bit low on the initial rarefaction, and therefore mass conservation requires a somewhat smeared shock near  $x = 0.4$ . However, the two pulses merge smoothly into a single monotonic pulse by  $t = 0.5$ .

For the coarsest discretization,  $h = 1/40 = 0.025$  and  $\Delta t = 1/80$ , the shock at  $t = 0.3$  and  $x = 0.4$  is quite smeared. This is due possibly, at least partly, to the very coarse discretization used. Note that in this case only two elements resolve the initial downward sloping pulse of the initial condition over  $[0, 0.05]$ , and only six elements resolve the square pulse at  $[0.25, 0.4]$ . In our experience, even for linear convection-diffusion problems, Eulerian–Lagrangian methods have typically needed three to four elements to resolve the shape of a steep front accurately.

The  $L_1$  errors are given in Table 6.1. For the same spatial resolution  $h = 1/80$ , the traceline and CWENO-5 solutions are of similar accuracy, even though the traceline method uses a time step three times larger. Overall, it should be expected that the traceline method, which is formally only second order accurate, is worse than

TABLE 6.1

Ex. 4.  $L_1$  errors at various times for the traceline and CWENO-5 methods, and the total CPU time in seconds.

Time	Traceline	Traceline	CWENO-5
	$h = 1/40$ $\Delta t = 1/80$	$h = 1/80$ $\Delta t = 1/160$	$h = 1/80$ $\Delta t = 1/480$
0.1	0.0159	0.0101	0.0098
0.2	0.0202	0.0089	0.0077
0.3	0.0175	0.0085	0.0100
0.4	0.0223	0.0132	0.0094
0.5	0.0154	0.0096	0.0091
CPU Time	7.86E-02	1.95E-01	4.40E-03

CWENO-5 on this example, since CWENO-5 is fifth order. Despite the traceline method being low order accurate, it shows comparable numerical diffusion (note the especially good approximation at the trailing edge of the rarefaction at  $t = 0.1$  around  $x = 0.25$ ). A formally higher order version of the type of scheme presented here for the linear transport system has been developed [24, 17]. We expect to be able to extend the ideas to the nonlinear traceline method.

It is true that the traceline method requires more computation time. It is a matter of further research to speed up the computation. Nevertheless, we have achieved our main objective of using long time steps.

**6.2. Burgers' equation.** In the second set of numerical tests, we study the propagation of jump discontinuities for the classic Burgers' equation

$$(6.8) \quad s_t + f(s)_x = 0, \quad x \in (0, 1), t \in (0, 1),$$

$$(6.9) \quad z_t + F(z)_x = 0, \quad x \in (0, 1), t \in (0, 1),$$

where  $s + z = 1$  and

$$(6.10) \quad f(s) = \frac{s^2}{2}$$

is a convex flux function. Again,  $F(z) = u - f(s)$  and  $F(0) = 0$  implies  $u = f(1) = 1/2$ , so

$$(6.11) \quad F(z) = \frac{1}{2} - \frac{(1-z)^2}{2} = \frac{2z - z^2}{2},$$

which is concave. In this example, the characteristic speed is  $f'(s) = s$ , while the wetting traceline speed is only  $f(s)/s = s/2$ . The maximal characteristic speed is  $f'(1) = 1$ , so the general CFL time step limit is

$$\Delta t_{\text{CFL}} = h.$$

**6.2.1. Example 5.** In this example, we study Burgers' equation with an initial shock with left state  $s_L$  less than the right state  $s_R$ . More precisely, the initial condition is given as

$$s = \begin{cases} s_L = 0.5 & \text{if } x < 0.55, \\ s_R = 1.0 & \text{if } x \geq 0.55, \end{cases}$$

where the jump is at  $x = 0.55$ . In this case, a rarefaction forms.

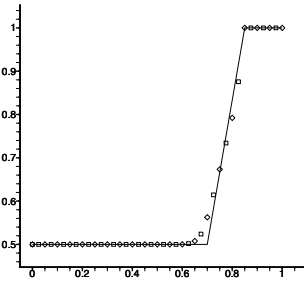


FIG. 6.13. Ex. 5. *Burgers' equation rarefaction formation with  $h = 1/20$  and  $\Delta t = 2h$ . The open diamonds are the grid concentration values, the open squares are the average element values, and the solid line is the true solution.*

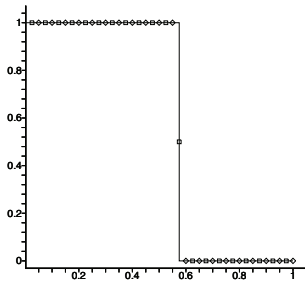


FIG. 6.14. Ex. 6. *Burgers' equation shock propagation with  $h = 1/20$  and  $\Delta t = 5h$ . The open diamonds are the grid concentration values, the open squares are the average element values, and the solid line is the true solution.*

We use only 20 grid elements, so  $h = 1/20$ , and  $\Delta t = 2h = 1/10$  (twice the CFL limit), and we plot the result at  $t = 3\Delta t = 0.3$  in Figure 6.13. The green squares are the grid concentration values, the blue squares are the average element values, and the red line is the true solution.

Wetting particles to the right (where  $s = 1$ ) travel with speed 0.5, while particles to the left (where  $s = 0.5$ ) travel only with speed 0.25, and thus a rarefaction forms. However, the jump itself travels at characteristic speeds, and so the right side point, where  $s$  becomes 1, travels as  $x_R(t) = 0.55 + t = 0.85$ , and the left point, where  $s$  changes from 0.5, travels as  $x_L(t) = 0.55 + t/2 = 0.7$ . Even though we follow traceline speeds and use no knowledge of the true solution, the method allows the rarefaction to form properly.

**6.2.2. Example 6.** In this example, we study Burgers' equation with a left state  $s_L$  greater than the right state  $s_R$ ; that is, with the initial condition

$$s = \begin{cases} s_L = 1 & \text{if } x < 0.2, \\ s_R = 0 & \text{if } x \geq 0.2, \end{cases}$$

where the jump is now at  $x = 0.2$ . In this case, the shock persists in time.

Again we use  $h = 1/20$  and  $\Delta t = 5h = 1/4$ , which is 5 times the CFL limited time step. We run to  $t = 3\Delta t = 0.75$ . The shock speed is  $\frac{1}{2}(s_R + s_L) = 0.5$ , so the shock will reach  $0.2 + 0.5t = 0.575$ . We plot the result in Figure 6.14. The example shows that our scheme can propagate the shock at the proper speed in Burgers' equation. We emphasize that we have followed traceline speeds in the particle traceback computations, not characteristic speeds, and we used no knowledge of the true solution in this example.

**6.2.3. Example 7.** We now study Burgers' equation with a combination of a shock and a rarefaction. The initial condition is given as

$$s = \begin{cases} 0.5 & \text{if } x \leq 0.3, \\ 1.0 & \text{if } 0.3 < x \leq 0.75, \\ 0.5 & \text{if } x > 0.75. \end{cases}$$

The true solution gives a rarefaction between  $0.3 + 0.5t$  and  $0.3 + t$  and a shock at  $0.75 + 0.75t$ .

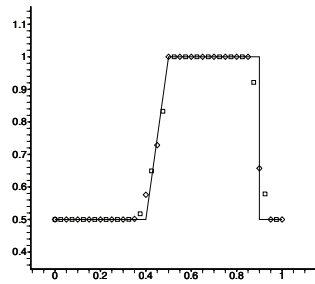


FIG. 6.15. Ex. 7. Burgers' equation with both a rarefaction and shock. We use  $h = 1/20$  and  $\Delta t = 2h$ . The open diamonds are the grid concentration values, the open squares are the average element values, and the solid line is the true solution.

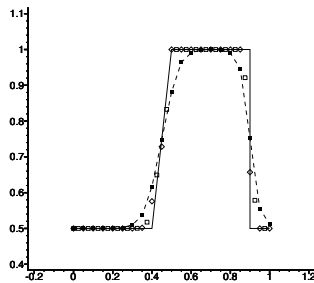


FIG. 6.16. Ex. 7. Burgers' equation with both a rarefaction and shock. We use  $h = 1/20$  and  $\Delta t = 2h$ . The open diamonds are the grid concentration values, the open squares are the average element values, and the solid line is the true solution. The solid squares and dashed line are the CWENO-5 result with  $h = 1/20$  and  $\Delta t = 1/100 = 0.2\Delta t_{CFL}$ .

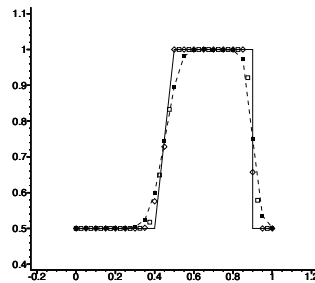


FIG. 6.17. Ex. 7. Burgers' equation with both a rarefaction and shock. We use  $h = 1/20$  and  $\Delta t = 2h$ . The open diamonds are the grid concentration values, the open squares are the average element values, and the solid line is the true solution. The solid squares and dashed line are the CWENO-5 result with  $h = 1/20$  and  $\Delta t = 1/50 = 0.4\Delta t_{CFL}$ .

Again we use  $h = 1/20$  and  $\Delta t = 2h = 1/10$ . This time the results are given at time  $t = 2\Delta t = 0.2$  and shown in Figure 6.15. As can be seen, the method has no trouble handling a complex shock-rarefaction structure.

We continue by comparing results to those produced by the CWENO-5 scheme. We use the same  $h = 1/20$  and  $\Delta t = 1/10 = 2\Delta t_{CFL}$  for our scheme in all tests. For the CWENO-5 scheme we make four different tests. We use the same  $h = 1/20$  and also  $h = 1/40$ , as well as much shorter time steps  $\Delta t = 0.2\Delta t_{CFL} = 0.2h$  and  $\Delta t = 0.4\Delta t_{CFL} = 0.4h$ .

Results are shown in Figures 6.16–6.19. Clearly the new traceline method outperforms CWENO-5 at the rarefaction edge ( $x \approx 0.5$ ). Both methods perform well near the shock. Our new method is perhaps better when the spatial resolution agrees (at  $h = 1/20$ , Figures 6.16–6.17), and the two methods are perhaps comparable when CWENO-5 alone uses the finer resolution  $h = 1/40$  (Figures 6.18–6.19). Even though the traceline method is a low order method, it works well, especially on the type of coarse grids one would expect to compute over in porous medium applications.

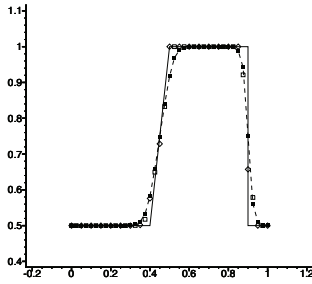


FIG. 6.18. Ex. 7. Burgers' equation with both a rarefaction and shock. We use  $h = 1/20$  and  $\Delta t = 2h$ . The open diamonds are the grid concentration values, the open squares are the average element values, and the solid line is the true solution. The solid squares and dashed line are the CWENO-5 result with  $h = 1/40$  and  $\Delta t = 1/200 = 0.2\Delta t_{CFL}$ .

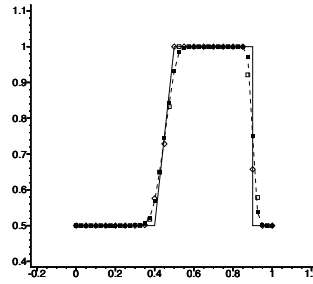


FIG. 6.19. Ex. 7. Burgers' equation with both a rarefaction and shock. We use  $h = 1/20$  and  $\Delta t = 2h$ . The open diamonds are the grid concentration values, the open squares are the average element values, and the solid line is the true solution. The solid squares and dashed line are the CWENO-5 result with  $h = 1/40$  and  $\Delta t = 1/100 = 0.4\Delta t_{CFL}$ .

**6.2.4. Example 8.** In this example, we study Burgers' equation on a problem involving the merging of two shocks. The initial condition is

$$s = \begin{cases} 1 & \text{if } x < 0.25, \\ 0.5 & \text{if } 0.25 < x \leq 0.5, \\ 0 & \text{if } 0.5 \leq x, \end{cases}$$

and so the first shock initially at  $x = 0.25$  travels with speed 0.75, while the second shock initially at  $x = 0.5$  has speed 0.25. The two shocks merge at time  $t = 0.5$  at the position  $x = 0.625$ .

We use  $h = 1/20$ , and we compute the solution for two values of  $\Delta t$ , both larger than the CFL limit value  $\Delta t_{CFL} = h$ . In the first test, we take  $\Delta t = (10/3)h = 1/6$ , so that the two shocks merge at exactly step 3. We plot the result in Figure 6.20, showing the initial condition, the first step before the shocks merge, the third step as they merge, and the fourth step as they propagate as a single shock. The results show an almost perfect match to the true solution, even though no direct knowledge of the existence of shocks was used in the computation.

Similar results are seen in the second test using  $\Delta t = 3h = 0.15$ . In this test, the merging of the shocks at  $t = 0.5$  takes place between time step 3 ( $t = 0.45$ ) and step 4 ( $t = 0.6$ ). Nevertheless, the results shown in Figure 6.21 give again an almost perfect match to the true solution.

**6.2.5. Example 9.** The final test involving Burgers' equation uses a smooth initial condition, namely

$$u(x, 0) = 0.75 + 0.25 \sin(\pi x),$$

on the interval  $[0, 2]$ . A shock forms at time  $4/\pi$ . The  $L_1$  and  $L_\infty$  errors for several test runs are given in Table 6.2 at time  $t = 1.0 < 4/\pi = 1.27$  before the shock forms. It is clear that our traceline scheme provides comparable results with CWENO-5 when using coarse grids of size  $h = 2/20$  and  $H = 2/10$ . The traceline time step is relatively large, being 5 and 10 times the CFL limit of  $\Delta t = h$  or  $H$ .

Of course, the CWENO-5 scheme converges much faster than our scheme, since it is formally a fifth order scheme in space while ours is only second order. It is also

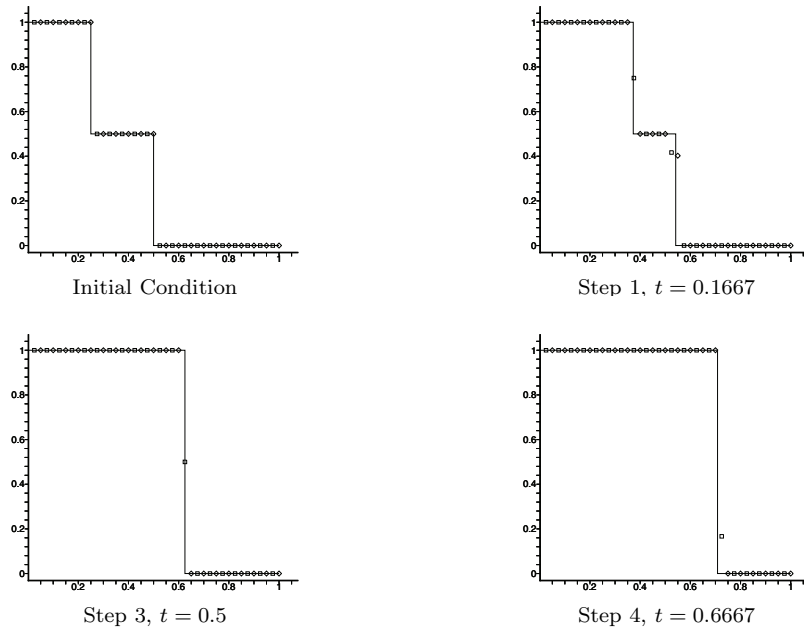


FIG. 6.20. Ex. 8. Burgers' equation with two merging shocks, using  $h = 1/20$  and  $\Delta t = (10/3)h$ . The open diamonds are the grid concentration values, the open squares are the average element values, and the solid line is the true solution. The shocks merge exactly at Step 3.

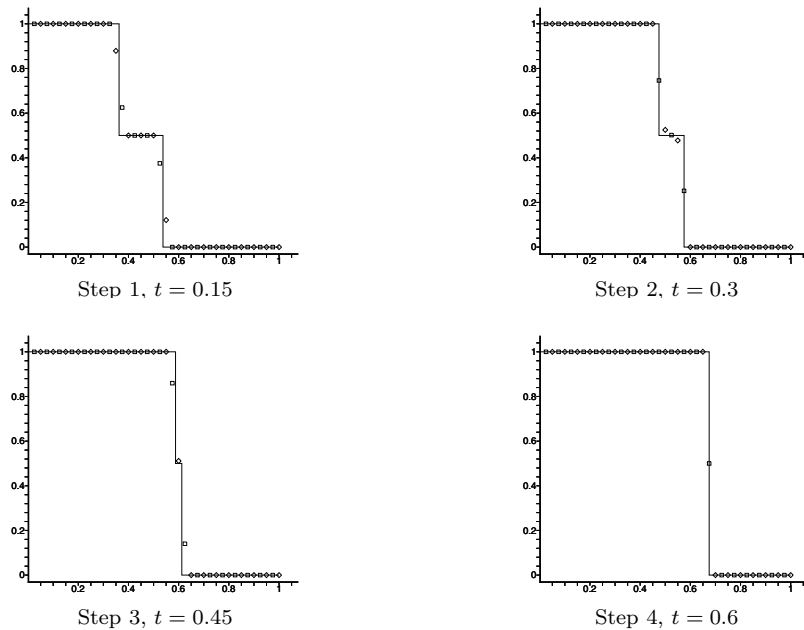


FIG. 6.21. Ex. 8. Burgers' equation with two merging shocks at  $t = 0.5$ , using  $h = 1/20$  and  $\Delta t = 3h$ . The open diamonds are the grid concentration values, the open squares are the average element values, and the solid line is the true solution. The shocks merge between Steps 3 and 4.

TABLE 6.2  
*Ex. 9. Errors for  $h = 2/20$ ,  $H = 2/10$  at time  $t = 1.0$ .*

Method	Time step	$L_1$ error	$L_\infty$ error	CPU time (sec.)
Traceline	$5h$	1.104E-02	3.143E-02	1.504E-03
Traceline	$10h$	2.050E-02	4.338E-02	7.611E-04
Traceline	$5H$	3.683E-02	7.602E-02	3.635E-04
CWENO-5	$0.2h$	1.116E-02	4.026E-02	3.487E-04
CWENO-5	$0.1h$	1.628E-02	5.038E-02	6.826E-04

difficult to compare run times obtained from disparate codes, since so many coding issues affect the results. Nevertheless, we observe that the timings and accuracy for this example are comparable between the two methods. Our method is more costly per step, but it does allow for larger time steps that exceed the CFL limit. We maintain hope that further developments can be found for the general traceline method to make it more effective, such as the development of a higher order version (for work in this direction, see, e.g., [24, 17]).

Currently, it is not clear whether the traceline method presented here could be faster than CWENO-5 on this smooth example. However, the traceline method realizes an advantage in terms of its application to nonsmooth problems and its use in parallel computation. In general, it appears that the traceline method can allow much coarser grids in the nonsmooth case (as the previous numerical results show, e.g., Figures 6.16–6.19). The combination of being free from CFL constraints and using coarser grids implies that the traceline method can use a time step greatly exceeding the time step of a CFL limited method that needs a fine spatial grid to get into the asymptotic region of the convergence for nonsmooth problems. Traceline methods therefore need less computer memory. CFL limited methods also suffer in parallel computation, since time stepping is essentially a serial in time process. Our traceline method beats the CFL limit and increases the amount of local computation. It can therefore make more efficient use of additional processors in parallel computation.

**6.3. A linear equation: Example 10.** In our last example, we discuss approximation of the linear equation

$$(6.12) \quad s_t + s_x = 0, \quad x \in (0, 2), \quad t \in (0, 1),$$

$$(6.13) \quad z_t + z_x = 0, \quad x \in (0, 2), \quad t \in (0, 1),$$

where  $s + z = 1$ . In this example,  $f(s) = s$  and  $F(z) = 1 - s = z$ , so the characteristic speed is  $f'(s) = 1$ , and the wetting traceline speed is also  $f(s)/s = 1$ . The general CFL time step limit is

$$\Delta t_{\text{CFL}} = h.$$

For a linear problem, the traceline method reduces to the characteristics-mixed method [1, 4, 2]. There is no CFL constraint, the traceline is the characteristic, it follows a straight line, and therefore the trace-back points are exact. As a consequence, our traceline method provides the exact solution up to resolution of the initial condition and projection back to the Eulerian grid. That is, the solution is a series of projections and translates of the approximated initial condition. Wang and Al-Lawatia [27] showed that Eulerian-Lagrangian methods outperform ENO/WENO schemes in the context of linear problems, so we do not repeat such results here.

Furthermore, if we choose time steps so that grid points trace to grid points, there is no projection error. In this case, our traceline method provides the exact solution

up to resolution of the initial condition. It gives a translate of the approximated initial condition at each time step. Obviously, in this case, our scheme is at worst comparable to and at best outperforms any other scheme on a linear problem. For example, interested readers can find less than perfect results for the WENO scheme as applied to Shu's linear test in [18]. Of course, WENO schemes were not designed for linear problems. Rather, WENO naturally handles much more general problems with complicated mathematical structure.

**7. Conclusions.** We developed a numerical approximation for a somewhat idealized system of two conservation laws in one space dimension modeling a simplified two-phase flow problem in a porous medium. The total fluid flow gives an overall total velocity for the system, which we assume has been solved. Then, either one of the original two equations provides the transport of one of the phases, such as the wetting phase.

The method transports wetting fluid mass by tracing the particle tracers, and so no CFL constraint arises. The main difficulty, however, was that it is not possible to follow individual tracers independently. Instead, we approximately trace along tracers using local mass conservation principles and self-consistency.

A major thesis of this work has been that the two-phase flow problem actually contains two mass conservation principles, one for each phase. Even though we need approximately only one of the two original equations, we still must respect both conservation principles. Our numerical method does so over the computational mesh (i.e., locally), and so is a fully conservative Eulerian–Lagrangian tracer method.

This conceptual framework generalizes in principle to more complex multiphase multicomponent systems in higher dimensions; we expect that the fully conservative property will be crucial in accurate tracer-based approximations of such systems. For example, we mention two possible approaches to handling the multidimensional problem. First is the possible use of a standard Strang splitting [26] in space, accounting first for the  $x$ -velocity transport and then the  $y$ -velocity transport (and then  $z$ , in three dimensions). Such an approach decouples the problem into the type of one-dimensional problems treated in this paper. Second, two of the authors plus a collaborator have investigated a stream-tube approach for the linear transport system, which requires only one-dimensional solutions along the tube [3]. We expect to investigate extensions of this approach to the two-phase system.

The numerical results demonstrate the ability of the method to handle accurately problems with shocks and rarefactions, and to do so on very coarse spatial grids and with time steps larger than the CFL limit.

**Acknowledgments.** The authors thank Professor Jianxian Qiu for helpful discussions regarding the CWENO scheme, and for providing the source code of his implementation of CWENO-5 [9].

#### REFERENCES

- [1] T. ARBOGAST, A. CHILAKAPATI, AND M. F. WHEELER, *A characteristic-mixed method for contaminant transport and miscible displacement*, in *Computational Methods in Water Resources IX*, Vol. 1: Numerical Methods in Water Resources, T. F. Russell et al., eds., Computational Mechanics Publications, Southampton, UK, 1992, pp. 77–84.
- [2] T. ARBOGAST AND C.-S. HUANG, *A fully mass and volume conserving implementation of a characteristic method for transport problems*, *SIAM J. Sci. Comput.*, 28 (2006), pp. 2001–2022.

- [3] T. ARBOGAST, C.-S. HUANG, AND C.-H. HUNG, *A Fully Conservative Eulerian-Lagrangian Stream-Tube Method for Advection-Diffusion Problems*, SIAM J. Sci. Comput., accepted.
- [4] T. ARBOGAST AND M. F. WHEELER, *A characteristics-mixed finite element method for advection dominated transport problems*, SIAM J. Numer. Anal., 32 (1995), pp. 404–424.
- [5] J. BEAR, *Dynamics of Fluids in Porous Media*, Dover, New York, 1972.
- [6] J. B. BELL, C. N. DAWSON, AND G. R. SHUBIN, *An unsplit higher-order Godunov scheme for scalar conservation laws in two dimensions*, J. Comput. Phys., 74 (1988), pp. 1–24.
- [7] M. A. CELIA, T. F. RUSSELL, I. HERRERA, AND R. E. EWING, *An Eulerian-Lagrangian localized adjoint method for the advection-diffusion equation*, Adv. in Water Res., 13 (1990), pp. 187–206.
- [8] Z. CHEN, G. HUAN, AND Y. MA, *Computational Methods for Multiphase Flows in Porous Media*, Comput. Sci. Eng. 2, SIAM, Philadelphia, 2006.
- [9] COMPUTATIONAL FLUID DYNAMICS LABORATORY, *One dimension Burgers Equation by 5th order CWENO*, State Key Laboratory of Scientific and Engineering Computing (LSEC), Institute of Computational Mathematics, Chinese Academy of Sciences, source code file cweno\_bur.f; available online at <http://lsec.cc.ac.cn/lcfd/> (2001).
- [10] H. K. DAHLE, R. E. EWING, AND T. F. RUSSELL, *Eulerian-Lagrangian localized adjoint methods for a nonlinear advection-diffusion equation*, Comput. Methods Appl. Mech. Engrg., 122 (1995), pp. 223–250.
- [11] C. N. DAWSON, T. F. RUSSELL, AND M. F. WHEELER, *Some improved error estimates for the modified method of characteristics*, SIAM J. Numer. Anal., 26 (1989), pp. 1487–1512.
- [12] J. DOUGLAS, JR. AND C.-S. HUANG, *The convergence of a locally conservative Eulerian-Lagrangian finite difference method for a semilinear parabolic equation*, BIT, 41 (2001), pp. 480–489.
- [13] J. DOUGLAS, JR., F. PEREIRA, AND L.-M. YEH, *A locally conservative Eulerian-Lagrangian numerical method and its application to nonlinear transport in porous media*, Comput. Geosci., 4 (2000), pp. 1–40.
- [14] J. DOUGLAS, JR. AND T. F. RUSSELL, *Numerical methods for convection-dominated diffusion problems based on combining the method of characteristics with finite element or finite difference procedures*, SIAM J. Numer. Anal., 19 (1982), pp. 871–885.
- [15] R. E. EWING, T. F. RUSSELL, AND M. F. WHEELER, *Convergence analysis of an approximation of miscible displacement in porous media by mixed finite elements and a modified method of characteristics*, Comput. Methods Appl. Mech. Engrg., 47 (1984), pp. 73–92.
- [16] M. W. FARTHING, C. E. KEES, T. F. RUSSELL, AND C. T. MILLER, *An ELLAM approximation for advective-dispersive transport with nonlinear sorption*, Adv. in Water Res., 29 (2006), pp. 657–675.
- [17] C.-S. HUANG, T. ARBOGAST, AND J. QIU, *An Eulerian-Lagrangian WENO finite volume scheme for advection problems*, J. Comput. Phys., 231 (2012), pp. 4028–4052.
- [18] G.-S. JIANG AND C.-W. SHU, *Efficient implementation of weighted ENO schemes*, J. Comput. Phys., 126 (1996), pp. 202–228.
- [19] C. T. LAWRENCE AND A. L. TITS, *Nonlinear equality constraints in feasible sequential quadratic programming*, Optim. Methods Softw., 6 (1996), pp. 265–282.
- [20] R. J. LEVEQUE, *Numerical Methods for Conservation Laws*, 2nd ed., Birkhäuser Verlag, Basel, 1992.
- [21] D. W. PEACEMAN, *Fundamentals of Numerical Reservoir Simulation*, Elsevier, Amsterdam, 1977.
- [22] O. PIRONNEAU, *On the transport-diffusion algorithm and its applications to the Navier-Stokes equations*, Numer. Math., 38 (1981/82), pp. 309–332.
- [23] J. QIU AND C.-W. SHU, *On the construction, comparison, and local characteristic decomposition for high-order central WENO schemes*, J. Comput. Phys., 183 (2002), pp. 187–209.
- [24] J.-M. QIU AND C.-W. SHU, *Conservative high order semi-Lagrangian finite difference WENO methods for advection in incompressible flow*, J. Comput. Phys., 230 (2011), pp. 863–889.
- [25] T. F. RUSSELL, B.-O. HEIMSUND, H. K. DAHLE, AND M. S. ESPEDAL, *Adjoint Methods are Particle Methods*, to appear.
- [26] G. STRANG, *On the construction and comparison of difference schemes*, SIAM. J. Numer. Anal., 5 (1968), pp. 506–517.
- [27] H. WANG AND M. AL-LAWATIA, *A comparison of ELLAM with ENO/WENO schemes for linear transport equations*, in Numerical Treatment of Multiphase Flows in Porous Media, Lecture Notes in Phys. 552, Springer, Berlin, 2000, pp. 311–323.
- [28] H. WANG AND M. AL-LAWATIA, *A locally conservative Eulerian-Lagrangian control-volume method for transient advection-diffusion equations*, Numer. Methods Partial Differential Equations, 22 (2006), pp. 577–599.

- [29] H. WANG, D. LIANG, R. E. EWING, S. L. LYONS, AND G. QIN, *An ELLAM approximation for highly compressible multicomponent flows in porous media. Locally conservative numerical methods for flow in porous media*, *Comput. Geosci.*, 6 (2002), pp. 227–251.
- [30] H. WANG, W. ZHAO, AND R. E. EWING, *A numerical modeling of multicomponent compressible flows in porous media with multiple wells by an Eulerian-Lagrangian method*, *Comput. Vis. Sci.*, 8 (2005), pp. 69–81.
- [31] J. L. ZHOU AND A. TITS, *User's Guide for FFSQP Version 3.7: A Fortran Code for Solving Optimization Programs, Possibly Minimax, with General Inequality Constraints and Linear Equality Constraints, Generating Feasible Iterates*, Technical report SRC-TR-92-107r5, Institute for Systems Research, University of Maryland, College Park, MD, 1997.